PHYSICAL REVIEW A **105**, 062817 (2022)

Differential and integral cross sections for the valence-shell excitations in D_2O studied by fast electron impact

Zi-Ru Ma,[1] Shu-Xing Wang,[1,*] Yi-Geng Peng,[2,3] Jian-Hui Zhu,[1] Yuan-Chen Xu,[1] Xiao-Jiao Du,[1] Li-Han Wang,[1]
Wei-Qing Xu,[4] Yong Wu,[3,5,†] Jian-Guo Wang,[3] and Lin-Fan Zhu[1,‡]
[1]*Department of Modern Physics, University of Science and Technology of China, Hefei, Anhui 230026, China*
[2]*Department of Applied Physics, Nanjing University of Science and Technology, Nanjing 210094, China*
[3]*Institute of Applied Physics and Computational Mathematics, Beijing 100088, China*
[4]*Center for Transformative Science, ShanghaiTech University, Shanghai 201210, China*
[5]*HEDPS, Center for Applied Physics and Technology, and College of Engineering, Peking University, Beijing 100871, China*

(Received 21 April 2022; accepted 8 June 2022; published 22 June 2022)

The experimental generalized oscillator strengths (GOSs) for the valence-shell excitations of heavy water in 6.50–12.17 eV are determined by fast electron scattering with an incident electron energy of 1500 eV and an energy resolution of 80 meV. The experimental data of the $\tilde{A}\,^1B_1 \leftarrow \tilde{X}\,^1A_1$ transition between H_2O and D_2O show significant discrepancies around the minimum, and further theoretical calculations with nuclear effects accounted are recommended. The comparisons of the present GOSs of $\tilde{A}\,^1B_1 \leftarrow \tilde{X}\,^1A_1$ and $\tilde{B}\,^1A_1 \leftarrow \tilde{X}\,^1A_1$ transitions in D_2O with theoretical calculations within the first Born approximation and the second Born approximation indicate that the higher Born terms become prominent at large momentum transfers. In particular, the GOSs of the dipole-forbidden transition $^1A_2 \leftarrow \tilde{X}\,^1A_1$ are extracted, benefiting from the present high-energy electron scattering, where most of electronic dipole-forbidden transitions are not involved. By extrapolating the GOSs to the zero momentum transfer, the optical oscillator strengths for the corresponding dipole-allowed transitions are determined, which provide an independent cross-check for previous optical measurements. Moreover, the integral Born cross sections are scaled to an accurate level with the aid of the binding energy–excitation energy–scaling method. The relevant experimental data in this work can supplement the molecular database with electron collision data involving heavy water.

DOI: 10.1103/PhysRevA.105.062817

I. INTRODUCTION

Electron collisions involving water molecules are of great importance in many applied sciences due to their essential role in biological, atmospheric, and astrophysical environments. Heavy water (D_2O) forms when hydrogen atoms in water are replaced by deuterium and constitutes the most important isotopic molecules of water. D_2O has many applications in disease treatment, drug research [1], and isotope dilution experiments [2]. The discovery of D_2O in the interstellar medium [3] offered an opportunity to address the earliest phases of star formation by tracing the deuterium fractionation. Therefore, the knowledge of electronic structure and cross-section data is valuable for identifying and modeling D_2O in the astronomical environments. For example, photochemical reactions with deuterated and nondeuterated water are essential for understanding the formation and evolution of interstellar molecules [4]. Optical oscillator strength densities, or the equivalent photoabsorption cross sections, are fundamental input data for calculating the photolysis rates in the planetary atmosphere [5]. The photoinduced fractionation of isotopic molecules will lead to an unusual [D]/[H] isotopic ratio, also known as deuterium enrichment, in planetary atmospheres [5,6]. Furthermore, D_2O is one of the simplest triatomic molecules, constituting an ideal system for testing theoretical methods and computational codes. Notably, isotopic effects usually alter the physical and chemical properties to some extent, which is also attractive in theoretical investigations.

The electronic configuration of molecular water in the C_{2v} ground state is $(1a_1)^2(2a_1)^2(1b_2)^2(3a_1)^2(1b_1)^2$ $(\tilde{X}\,^1A_1)$. The electronic structure of D_2O has been extensively studied by optical methods [7–10], and photoabsorption cross sections have been reported by Katayama *et al.* [11], Gürtler *et al.* [12], Lee and Suto [13], and Fillion *et al.* [14]. Notably, the most recent cross sections measured by Fillion *et al.* [14] differ from the other data significantly. Furthermore, the calculated absorption cross sections for D_2O are only available in the energy range 8.6–9.9 eV [15]. However, the differential cross sections (DCSs) and integral cross sections (ICSs) for electron impact excitations in D_2O are still not available. Note that the DCSs or the related generalized oscillator strengths (GOSs) can provide information on the wave functions of the initial and final states. The definition of GOS for an electronic excitation was proposed by Bethe [16] to describe the transition probability of the inelastic scattering of fast charged

---

[*] wangshuxing@ustc.edu.cn
[†] wu_yong@iapcm.ac.cn
[‡] lfzhu@ustc.edu.cn

particles by atoms and molecules as

$$f(E_n,\mathbf{K})=\frac{2E_n}{K^2}\left|\langle\Psi_n|\sum_{j=1}^{N}\exp(i\mathbf{K}\cdot\mathbf{r}_j)|\Psi_0\rangle\right|^2. \tag{1}$$

Here E_n and $\mathbf{K}$ are the excitation energy and momentum transfer, respectively, Ψ_0 and Ψ_n are the N-electron wave functions for the initial and final states, respectively, and $\mathbf{r}_j$ is the position vector of the jth electron.

Since GOS is only determined by the electronic structure of target atoms or molecules, accurate GOS can be used for precise evaluation of theoretical models and computational codes. The GOSs of the two low-lying excited states $\tilde{A}\,^1B_1$ and $\tilde{B}\,^1A_1$ in H_2O have been studied both experimentally and theoretically [17–21]. The higher-order Born terms were found to be appreciable in the GOS profiles around the minimum [21,22]. By comparing the GOSs between H_2O and D_2O, the isotopic effects on the electronic structures and the GOS profiles can be evaluated. Moreover, the measured GOS profile can be analytically expressed with the Lassettre formula by fitting the data [23–25]. Thus, the optical oscillator strengths (OOSs) for the corresponding dipole-allowed transitions can be extrapolated and the Born ICSs can be obtained by integrating the GOSs over the momentum transfer squares. Note that the Born ICSs are reliable for high impact electron energies when the Born approximation is valid. The gap between the low-energy and the high-energy electron scatterings was bridged by Kim [25,26] with the binding energy–excitation energy (BE)–scaling method. Since then, the ICSs for the dipole-allowed transitions have been available from the experimental GOSs with satisfactory accuracy.

In this work we report the experimental GOSs for the valence-shell excitations of D_2O in 6.50–12.17 eV by high-energy electron scattering. Absolute measurements were realized by using the crossed-beam-based relative flow technique. The OOSs for the corresponding excitations were also obtained by extrapolating the measured GOSs at the squared momentum transfer $K^2 \to 0$. In addition, the ICSs for the dipole-allowed excitations were derived according to the BE-scaling method. In Sec. II the experimental procedures and data analysis are presented in detail. The experimental data and comparisons with available data in the literature are discussed in Sec. III. We summarize the experimental results in Sec. IV.

II. EXPERIMENT AND DATA ANALYSIS

The high-resolution fast-electron energy-loss spectrometer used in this work has been described elsewhere [27,28] and the experimental procedure is outlined briefly here. The incident electron beam with an energy of 1500 eV is crossed with the sample at an angle of 90°. The energy resolution of the experimental spectrum of 80 meV results from a combination of the hemispherical monochromator and analyzer, which are both operated at a pass energy of 25 eV. The rotatable analyzer facilitates the collection of scattered electrons at several angles between 1.5° and 7°. The relative flow technique [29,30] enables the absolute normalization of the measured DCSs for the electronic excitations in D_2O. During the measurements, the gas sample (D_2O) is purified by repeated freeze-pump-thaw cycles, mixed with the calibration gas He at fixed ratios, and finally is injected into the reaction chamber. The flow rate for D_2O at 4.7 sccm (where sccm denotes cubic centimeter per minute at STP) is controlled by a MKS vapor source mass flow controller 1150C, while the flow rates for He (1 sccm for angles less than 6° and 1.5 sccm for 6°–7°) are controlled by a normal MFC flow meter. The background and operating pressures inside the reaction chamber are about 5×10^{-5} and 5×10^{-3} Pa, respectively.

The spectral intensities from the ground states to the excited states in D_2O and the $2\,^1P_1$ state in He are determined by the least-squares fitting of the measured spectra. Note that the DCS for the $1s^2\,^1S_0 \to 1s2p\,^1P_1$ transition in He has been measured and calculated with a high accuracy [31–34]. According to the relative flow technique, the absolute DCSs for the excitations in D_2O can be normalized to the data of $1s^2\,^1S_0 \to 1s2p\,^1P_1$ of He via

$$\frac{d\sigma_n(E_n,\theta)}{d\Omega}=\frac{\dot{n}_{\mathrm{He}}}{\dot{n}_{\mathrm{D_2O}}}\sqrt{\frac{M_{\mathrm{He}}}{M_{\mathrm{D_2O}}}}\frac{N_{\mathrm{D_2O}}(E_n,\theta)}{N_{\mathrm{He}}(E_{2p},\theta)}\frac{d\sigma_{\mathrm{He}}}{d\Omega}, \tag{2}$$

where $\dot{n}$ represents the flow rate, M refers to the molecular mass, and N is the intensity of the corresponding excitation. Within the framework of the first Born approximation (FBA), the measured DCS can be transformed into GOS via [35]

$$f(E_n,\mathbf{K})=\frac{E_n}{2}\frac{p_0}{p_a}K^2\frac{d\sigma_n}{d\Omega}. \tag{3}$$

Here p_0 and p_a are the magnitudes of incident and scattered electron momenta, respectively.

The experimental error sources on the measured GOSs include the finite angular resolution, the angle determination, the statistical counts, the least-squares fitting, and the absolute normalization. The total experimental errors are estimated to be less than 15% for the data at scattering angles less than 6° and about 25% for larger scattering angles.

The resulting GOS data are analytically expressed with the equation

$$f(E_n,\mathbf{K})=\frac{1}{(1+x)^6}\sum_{m=0}^{\infty}\frac{f_m x^m}{(1+x)^m}+axe^{-bx}. \tag{4}$$

Here the variable x is the scaled momentum transfer square, which is defined as $x=K^2/\alpha^2$. The scaling factor α^2 is treated as a fitting parameter as proposed by Kim [25,26]. The coefficients f_m are fitting parameters in which f_0 is the corresponding OOS for a dipole-allowed transition. The leading fraction in Eq. (4) is known as the Lassettre formula [23,24,36], while the exponential function with coefficients a and b is introduced to reproduce the secondary peak in the experimental GOS profile.

The analytical expression facilitates the integration of experimental GOS over the whole momentum transfer square region. The Born cross section at an incident electron energy E_0 is accessible through the integration

$$\sigma_{\mathrm{Born}}(E_0)=\frac{\pi}{E_0E_n}\int_{K^2_{\min}}^{K^2_{\max}}\frac{f(E_n,\mathbf{K})}{K^2}dK^2. \tag{5}$$

The lower and upper limits for the integration are $K^2_{\min}$ and $K^2_{\max}$, corresponding to the forward ($\theta=0°$) and backward

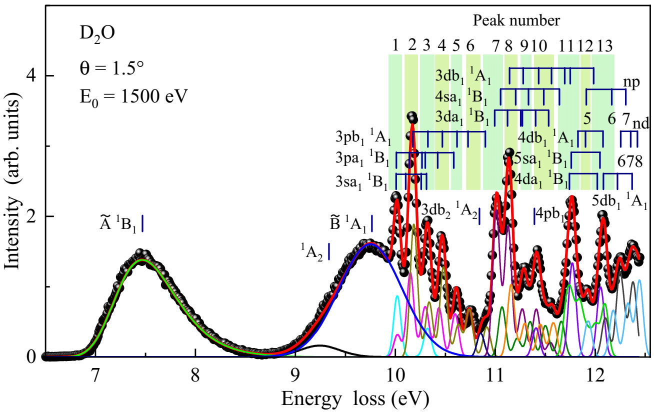

FIG. 1. Typical electron-energy-loss spectrum of D_2O measured at an incident energy of 1500 eV and a scattering angle of 1.5°. Black dots are the experimental data and solid lines are the fitted curves.

($\theta = 180^\circ$) scatterings under the incident electron energy E_0. The Born cross sections are accurate for the high incident electron energies where the Born approximation is applicable. However, the Born model usually underestimates the cross sections at low incident electron energies. The BE-scaling method based on the binary-encounter model was proposed by Kim [25,26] to bridge the gap between low-energy and high-energy scatterings. The BE-scaled ICS data can be derived according to the expression

$$\sigma_{\mathrm{BE}}(E_0) = \frac{E_0}{E_0 + B + E_n}\sigma_{\mathrm{Born}}(E_0), \tag{6}$$

where B is the binding energy of the electron being excited in an atom or a molecule.

III. RESULTS AND DISCUSSION

A typical electron-energy-loss spectrum of D_2O at a scattering angle of 1.5° is shown in Fig. 1 with the band assignments according to Refs. [8,9]. The first feature in the energy-loss spectrum of D_2O is ascribed to the transition $\tilde{A}\,^1B_1 \leftarrow \tilde{X}\,^1A_1$ at around 7.47 eV. The asymmetric line profile was reproduced by a Pearson IV function [37], which has been widely used for fitting asymmetric line shapes, e.g., in electron-energy-loss spectroscopy [38], x-ray-emission spectroscopy [39], and Raman spectroscopy [40]. The next feature consists of the dipole-forbidden transition $^1A_2 \leftarrow \tilde{X}\,^1A_1$ [41,42] and the dipole-allowed transition $\tilde{B}\,^1A_1 \leftarrow \tilde{X}\,^1A_1$ at 9.765 eV. The intensities for the second band were simulated by two Gaussian functions. Note that the dipole-forbidden transition $^1A_2 \leftarrow \tilde{X}\,^1A_1$ was not observed in earlier optical experiments. The transition energy and linewidth of $^1A_2 \leftarrow \tilde{X}\,^1A_1$ were determined by analyzing the energy-loss spectra at the large scattering angles since the transition intensities for the dipole-forbidden transitions are highlighted at the large momentum transfers. During the least-squares fitting, the spectral profile for the $\tilde{B}\,^1A_1 \leftarrow \tilde{X}\,^1A_1$ transition was fixed and the profile parameters for the $^1A_2 \leftarrow \tilde{X}\,^1A_1$ transition were treated as fitting coefficients. Similar treatment was adopted in fitting the energy-loss spectra of H_2O [21]. The averaged transition energy and linewidth for the $^1A_2 \leftarrow \tilde{X}\,^1A_1$ transition are 9.235 and 0.46 eV, respectively, which are close to the ones of H_2O ($E = 9.12$ eV and $\Delta E = 0.43$ eV) [21]. The broad spectral profiles of these transitions originate from their predissociative nature.

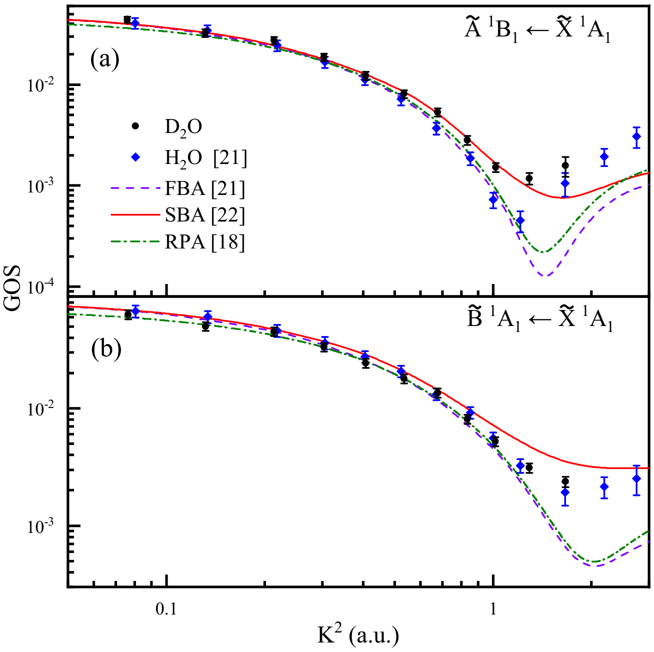

FIG. 2. The GOSs for the (a) $\tilde{A}\,^1B_1 \leftarrow \tilde{X}\,^1A_1$ and (b) $\tilde{B}^1A_1 \leftarrow \tilde{X}\,^1A_1$ transitions of D_2O, in comparison with the experimental and theoretical data of H_2O [18,21,22].

The higher-energy side (9.9–12.5 eV) of the energy-loss spectra stems from the promotions of $3a_1$ or $1b_1$ electrons into the Rydberg orbitals nsa_1, npa_1, npb_1, nda_1, ndb_1, and ndb_2 ($n = 3, 4, 5, \ldots$). The spectra are extremely complicated and the vibrational states are strongly overlapped. The transition assignments for the corresponding bands are presented in Fig. 1 and listed in Table I. The transition energies are set equal to the ones from Ref. [9] during the least-squares fitting. To avoid the uncertainties from the random intensity allocation between the nearby transitions with very narrow intervals, the spectra are divided into several bands and the yielded intensities for the transitions in the corresponding bands are added up to obtain the total DCSs [22].

A. Low-lying $\tilde{A}\,^1B_1$ and $\tilde{B}\,^1A_1$ states

The measured GOSs for the $\tilde{A}\,^1B_1 \leftarrow \tilde{X}\,^1A_1$ and $\tilde{B}\,^1A_1 \leftarrow \tilde{X}\,^1A_1$ transitions in D_2O are compared with the experimental and theoretical data of H_2O in Fig. 2, since there are no reference data for D_2O. The experimental GOSs have maxima at $K^2 = 0$ and decrease with increasing K^2, which is a typical characteristic of the dipole-allowed transitions. The experimental GOSs of $\tilde{A}\,^1B_1$ of D_2O are consistent with the measured data of H_2O [21] except for a few data points around the minimum. The discrepancies around the minimum might be attributed to the isotopic effect between H_2O and D_2O. Further theoretical calculations with nuclear effects accounted for are recommended to elucidate the difference. The calculated GOS profiles for H_2O were implemented by

TABLE I. Contributed transitions of the corresponding peaks labeled in Fig. 1. The excitation energies are adopted from Refs. [8,9].

Band No.	Transition	Energy (eV)
I	$3sa_1\,{}^1B_1(000)$	10.00
I	$3pa_1\,{}^1B_1(000)$	10.01
II	$3sa_1\,{}^1B_1(010)$	10.10
II	$3pa_1\,{}^1B_1(010)$	10.14
II	$3pb_1\,{}^1A_1(000)$	10.17
III	$3sa_1\,{}^1B_1(020)$	10.26
III	$3sa_1\,{}^1B_1(100)$	10.31
III	$3pa_1\,{}^1B_1(020)$	10.27
III	$3pa_1\,{}^1B_1(100)$	10.30
III	$3pb_1\,{}^1A_1(010)$	10.33
IV	$3pa_1\,{}^1B_1(110)$	10.42
IV	$3pb_1\,{}^1A_1(100)$	10.47
V	$3pa_1\,{}^1B_1(200)$	10.58
V	$3pb_1\,{}^1A_1(110)$	10.62
VI	$3db_2\,{}^1A_2(000)$	10.84
VI	$3pb_1\,{}^1A_1(200)$	10.73
VII	$3da_1\,{}^1B_1(000)$	10.99
VII	$4sa_1\,{}^1B_1(000)$	11.05
VII	$3pb_1\,{}^1A_1(210)$	10.90
VIII	$3da_1\,{}^1B_1(010)$	11.12
VIII	$3db_1\,{}^1A_1(000)$	11.14
VIII	$4sa_1\,{}^1B_1(010)$	11.20
IX	$3da_1\,{}^1B_1(020)$	11.25
IX	$3da_1\,{}^1B_1(100)$	11.27
IX	$3db_1\,{}^1A_1(010)$	11.28
IX	$4sa_1\,{}^1B_1(100)$	11.33
X	$3sa_1\,{}^1B_1(010)$	11.40
X	$3pa_1\,{}^1B_1(010)$	11.53
X	$3pa_1\,{}^1B_1(010)$	11.48
X	$3pa_1\,{}^1B_1(010)$	11.43
X	$3pa_1\,{}^1B_1(010)$	11.56
X	$3pa_1\,{}^1B_1(010)$	11.39
XI	$3da_1\,{}^1B_1(110)$	11.64
XI	$3da_1\,{}^1B_1(120)$	11.74
XI	$4sa_1\,{}^1B_1(110)$	12.02
XI	$3db_1\,{}^1A_1(100)$	11.69
XI	$3db_1\,{}^1A_1(110)$	11.75
XI	$4pb_1\,{}^1A_1(000)$	11.83
XII	$3db_1\,{}^1A_1(300)$	11.98
XII	$5pb_1\,{}^1A_1(000)$	12.08
XIII	$4db_1\,{}^1A_1(100)$	11.90
XIII	$4db_1\,{}^1A_1(110)$	12.08
XIII	$5sa_1\,{}^1B_1(000)$	11.76
XIII	$5sa_1\,{}^1B_1(100)$	12.05
XIII	$5db_1\,{}^1A_1(000)$	12.08
XIII	$6pb_1\,{}^1A_1(000)$	12.16

using the multireference single- and double-excitation configuration interaction (MRDCI) method within the FBA [21] and the second Born approximation (SBA) [22], and the random-phase approximation (RPA) approach within the FBA [18]. The calculations within the FBA [18,21] agree with the experimental data for K^2 below 1 a.u., while the higher Born terms become prominent around the minimum GOSs [22]. The simplified model within the SBA [22] significantly reduced the differences between the experiments and calculations, while the remaining disagreements may be attributed to the neglected intermediate excited states in the model and the contributions from the higher-order Born terms. Furthermore, it seems that the SBA works better for D_2O than for H_2O, especially for the $\tilde{A}\,{}^1B_1$ state. This might be due to the vibronic and isotopic effects. Further theoretical calculations with vibronic and isotropic effects are recommended to address this observation.

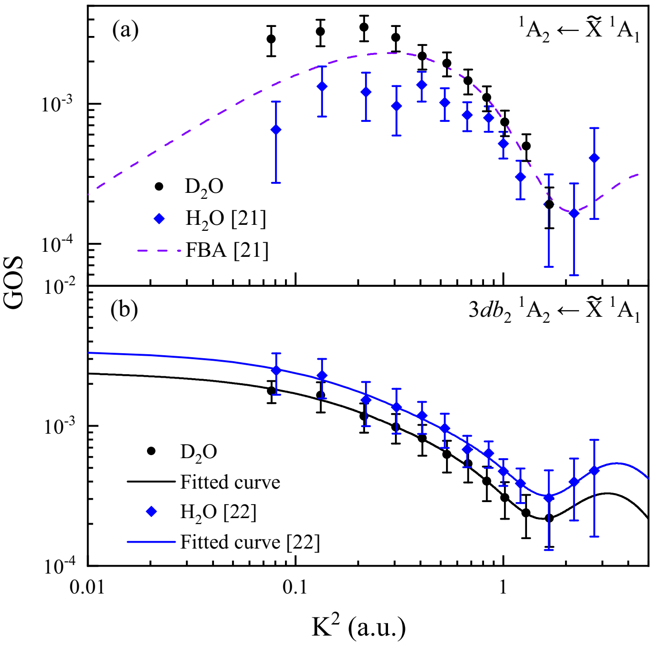

FIG. 3. The GOSs for the (a) $^1A_2 \leftarrow \tilde{X}\,{}^1A_1$ and (b) $3db_2\,{}^1A_2 \leftarrow \tilde{X}\,{}^1A_1$ transitions of D_2O and H_2O. The solid lines are the fitted results with Eq. (4).

The dipole-forbidden transition $^1A_2 \leftarrow \tilde{X}\,{}^1A_1$ cannot be easily approached by optical methods, while the momentum-transfer-dependent GOS can provide insight into the transition moments. The experimental GOSs for the $^1A_2 \leftarrow \tilde{X}\,{}^1A_1$ transition in D_2O are presented in Fig. 3(a) along with the

TABLE II. Optical oscillator strengths for the $\tilde{A}\,{}^1B_1 \leftarrow \tilde{X}\,{}^1A_1$ and $\tilde{B}\,{}^1A_1 \leftarrow \tilde{X}\,{}^1A_1$ transitions in D_2O and H_2O. The listed data are multiplied by a factor of 10^3. The numbers in parentheses are experimental uncertainties.

Source	$\tilde{A}\,{}^1B_1$	$\tilde{B}\,{}^1A_1$
	D_2O	
Present work	54.0(6.0)	74.0(8.0)
Photoabsorption [13]	46.0(5.0)	68.0(7.0)
Photoabsorption [47]	49.8(4.0)	
	H_2O	
Electron impact [21]	56.1(6.7)	85.4(10.3)
Dipole (e, e) [48]	49.7	73.2
Photoabsorption [49]	46.0	
MRDCI [21]	52.3	85.4

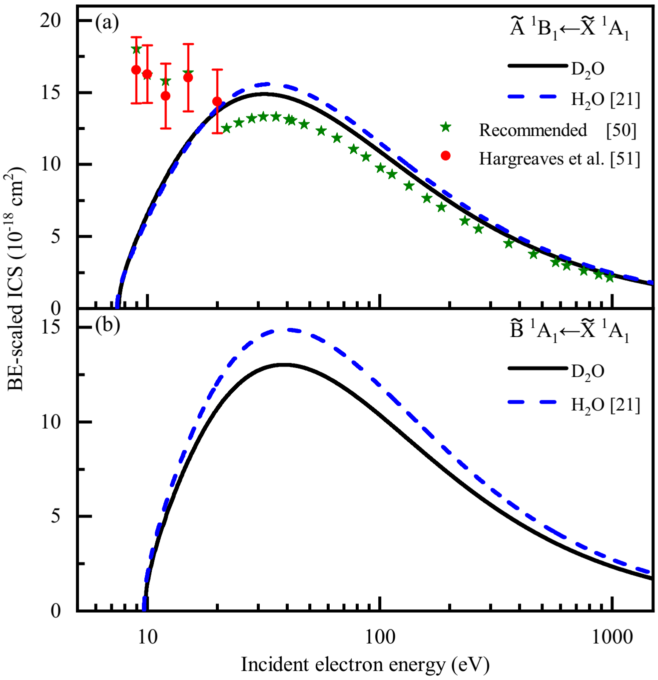

FIG. 4. The BE-scaled ICSs for the $\tilde{A}\,^1B_1$ and $\tilde{B}\,^1A_1$ states of D_2O and H_2O [21]. The green stars are the recommended data for electron impact excitation to the $\tilde{A}\,^1B_1$ state for H_2O [50]. The red circles are the experimental data obtained by low-energy electron scattering [51].

measured and calculated data for H_2O. The experimental GOSs increase with K^2 to reach a maximum at nonzero momentum transfer and then decrease with K^2. The present GOSs for D_2O differ from the ones of H_2O prominently while the data encounter large error bars due to the weak intensities and the heavy overlap with adjacent transitions. The FBA calculation [18] reproduces the experimental GOS profile well, and the differences in absolute scale are acceptable due to its large experimental uncertainties as mentioned above. Note that the discrepancies between the measured and calculated GOSs for the dipole-forbidden transitions have also been found in other targets [43–46]. Figure 3(b) shows the experimental GOS for a higher dipole-forbidden Rydberg transition $3db_2\,^1A_2 \leftarrow \tilde{X}\,^1A_1$ at 10.84 eV along with the fitted curve. However, the measured GOSs have a maximum at $K^2 = 0$ and decrease with increasing K^2, which is typical for dipole-allowed transitions. The heavy overlap with adjacent bands VI and VII should account for the abnormal phenomenon, which has also been pointed out in H_2O [22].

The extrapolated OOSs for the $\tilde{A}\,^1B_1 \leftarrow \tilde{X}\,^1A_1$ and $\tilde{B}\,^1A_1 \leftarrow \tilde{X}\,^1A_1$ transitions in D_2O are compared with the available data in Table II. The extrapolations are higher than the photoabsorption measurements [13] by 17% and 9%, respectively, while error bars can generally make up for the discrepancies. The latter measurement [47] of the photoabsorption cross sections for the $\tilde{A}\,^1B_1 \leftarrow \tilde{X}\,^1A_1$ transition is also in accord with the present extrapolation. The comparisons are also made with the experimental [21,48,49] and theoretical [21] data in Table II and general agreement is found between the data of D_2O and H_2O.

TABLE III. The DCSs for the labeled peaks shown in Fig. 1 and Table I (in units of a_0^2 sr^{-1}). The number in square brackets represents multiplication by the power of 10.

θ	$\tilde{A}\,^1B_1$	$\tilde{B}\,^1A_1$	I	II	III	IV	V	VI	VII	VIII	IX	X	XI	XII	XIII
1.5°	4.15[0]	4.59[0]	3.24[−1]	9.13[−1]	5.57[−1]	6.06[−1]	3.34[−1]	3.48[−1]	9.14[−1]	1.04[0]	5.67[−1]	8.80[−1]	1.29[0]	2.81[−1]	1.12[0]
2.0°	1.78[0]	2.10[0]	1.64[−1]	5.05[−1]	2.99[−1]	3.05[−1]	1.68[−1]	1.80[−1]	3.76[−1]	4.94[−1]	2.36[−1]	4.50[−1]	6.25[−1]	1.50[−1]	5.64[−1]
2.5°	9.24[−1]	1.17[0]	9.89[−2]	3.28[−2]	1.58[−1]	1.74[−1]	8.89[−2]	8.99[−2]	2.08[−1]	2.35[−1]	1.43[−1]	2.51[−1]	3.49[−1]	9.04[−2]	3.26[−1]
3.0°	4.43[−1]	6.10[−1]	5.88[−2]	2.00[−1]	8.88[−2]	1.02[−1]	4.82[−2]	5.18[−2]	9.65[−2]	1.21[−1]	7.08[−2]	1.50[−1]	1.88[−1]	5.68[−2]	1.87[−1]
3.5°	2.17[−1]	3.31[−1]	3.25[−2]	1.19[−1]	5.05[−2]	5.75[−2]	2.87[−2]	3.07[−2]	5.05[−2]	6.28[−2]	4.02[−2]	8.77[−2]	1.10[−1]	3.50[−2]	1.09[−1]
4.0°	1.09[−1]	1.86[−1]	2.03[−2]	7.62[−2]	2.90[−2]	3.58[−2]	1.64[−2]	1.84[−2]	3.03[−2]	3.58[−2]	2.16[−2]	5.57[−2]	6.66[−2]	2.23[−2]	6.86[−2]
4.5°	5.68[−2]	1.11[−1]	1.32[−2]	4.92[−2]	1.82[−2]	2.20[−2]	1.04[−2]	1.20[−2]	1.77[−2]	2.15[−2]	1.33[−2]	3.66[−2]	4.20[−2]	1.52[−2]	4.44[−2]
5.0°	2.43[−2]	5.39[−2]	7.09[−3]	2.83[−2]	9.73[−3]	1.26[−2]	5.58[−3]	7.14[−3]	9.88[−3]	1.14[−2]	7.95[−3]	2.14[−2]	2.42[−2]	8.81[−3]	2.59[−2]
5.5°	1.08[−2]	2.86[−2]	3.36[−3]	1.70[−2]	5.28[−3]	7.55[−3]	3.09[−3]	4.37[−3]	5.69[−3]	6.67[−3]	4.24[−3]	1.29[−2]	1.45[−2]	5.31[−3]	1.55[−2]
6.0°	6.60[−3]	1.34[−2]	1.56[−3]	8.88[−3]	2.83[−3]	4.23[−3]	1.71[−3]	2.64[−3]	3.54[−3]	4.16[−3]	2.02[−3]	7.32[−3]	7.83[−3]	2.71[−3]	8.45[−3]
7.0°	6.82[−3]	7.90[−3]	8.86[−4]	4.77[−3]	1.53[−3]	2.60[−3]	1.18[−3]	1.74[−3]	2.10[−3]	2.38[−3]	1.13[−3]	3.63[−3]	4.25[−3]	1.49[−3]	4.43[−3]

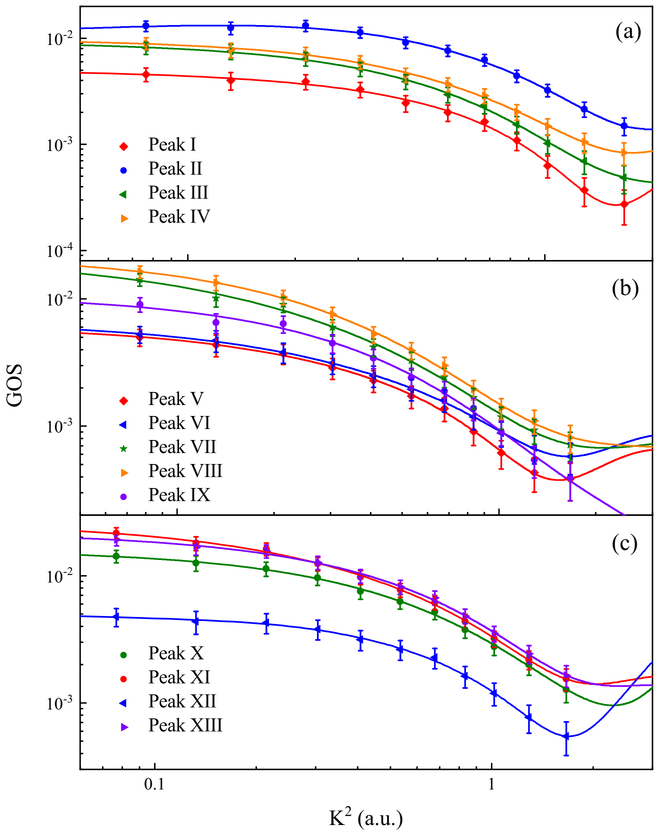

FIG. 5. The GOS for the excitations of D_2O in 9.93–12.17 eV. The peak numbers indicate the transition assignments as shown in Fig. 1 and Table I. The solid lines are the fitted curves according to Eq. (4).

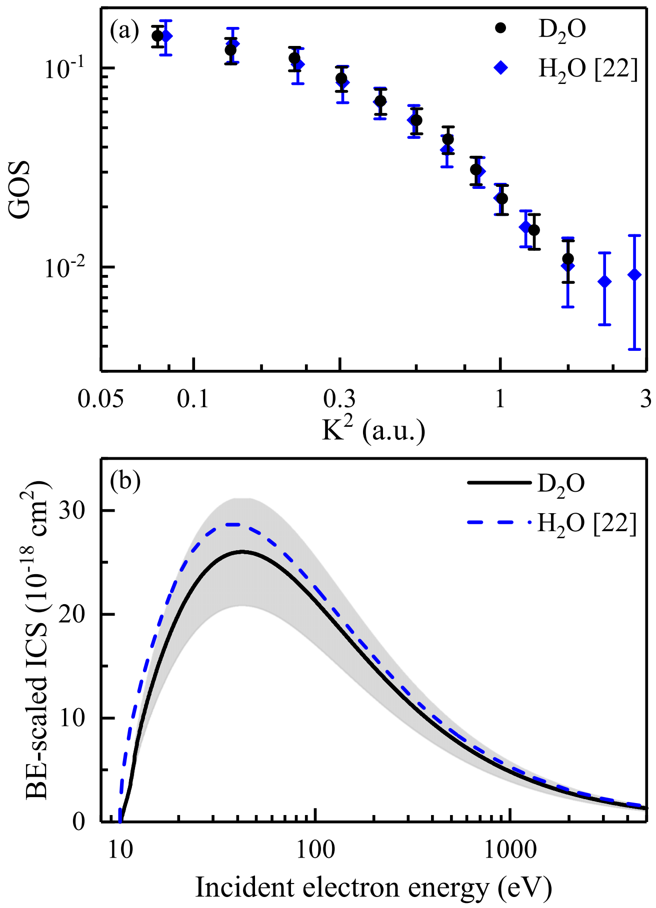

FIG. 6. Total (a) GOSs and (b) BE-scaled ICSs for the excitations in 9.93–12.17 eV of H_2O and D_2O. The gray areas indicate an estimated uncertainty of 20% on the ICS data.

TABLE IV. The OOSs for the excitations of D_2O in the range 9.93–12.17 eV and the corresponding peaks labeled in Fig. 1. The listed data are multiplied by a factor of 10^3. The numbers in parentheses are experimental uncertainties.

Band	Present work	Ref. [11]	Ref. [12]	Ref. [13]	Ref. [14]
I	5.1(0.8)			5.2(0.5)	
II	12.0(1.8)		14.0	10.0(1.0)	
III	9.5(1.4)		10.0	11.0(1.1)	
IV	9.9(1.5)		9.1	11.0(1.1)	
V	6.2(0.9)		6.4	5.3(0.5)	
VI	6.2(0.9)		5.9	4.5(0.5)	
VII	18.0(2.7)		17.0	20.0(2.0)	14.0
VIII	21.0(3.2)		14.0	19.6(2.0)	13.0
IX	11.0(1.7)		11.0	11.0(1.1)	4.6
X	16.0(2.4)		18.5	15.0(1.5)	9.5
XI	25.0(3.8)	22.0	21.0	21.0(2.1)	16.0
XII	5.7(0.9)	5.8	7.6	5.7(0.6)	1.9
XIII	22.0(3.3)	19.4	16.0	16.4(1.6)	13.0

The BE-scaled ICS data for the electron impact excitations to the $\tilde{A}\,{}^1B_1$ and $\tilde{B}\,{}^1A_1$ states of D_2O are compared with the data of H_2O [21] in Fig. 4. The derived ICSs for the $\tilde{A}\,{}^1B_1 \leftarrow \tilde{X}\,{}^1A_1$ excitation in D_2O and H_2O are consistent, while the ICSs for the $\tilde{B}\,{}^1A_1 \leftarrow \tilde{X}\,{}^1A_1$ excitation in D_2O are more than 10% lower than the data of H_2O. The discrepancies may be due to the fitting errors since the ${}^1A_2$ and $\tilde{B}\,{}^1A_1$ states are overlapped as shown in Fig. 1 and the extracted GOSs for the ${}^1A_2 \leftarrow \tilde{X}\,{}^1A_1$ excitation in D_2O and H_2O show a difference in the magnitude as presented in Fig. 3. Note that a recent review has compiled the cross sections for electron collisions with H_2O [50]. The BE-scaled ICS for the electron impact excitation to the $\tilde{A}\,{}^1B_1$ state in D_2O is also compared with the recommended data of H_2O in the review in [50] and the data of Hargreaves *et al.* [51] at lower collision energies. The recommended data at impact energies higher than 20 eV are 10% lower than the present data for D_2O. At lower incident electron energies, the recommendations are much higher than BE-scaled ICSs. The reason can be attributed to the fact that the exchange scattering, which contributes a great deal to low-energy scattering, cannot be accounted for by the BE-scaling method [25].

B. Higher bands

The measured DCSs for the transitions into higher bands of D_2O are listed in Table III and the derived GOSs are shown in Fig. 5. The experimental GOSs for the higher bands have maxima at zero momentum transfer and decrease with increasing K^2, indicating that these bands are dominated by

TABLE V. The BE-scaled ICSs (10^{-18} cm^2) of the corresponding peaks labeled in Fig. 1 of D_2O at different electron impact energies. The uncertainty on the derived ICS data is estimated to be less than 20%.

E_0 (eV)	$\tilde{A}\,^1B_1$	$\tilde{B}\,^1A_1$	I	II	III	IV	V	VI	VII	VIII	IX	X	XI	XII	XIII
12	9.11	5.00	0.47	1.69	0.60	0.68	0.29	0.31	0.39	0.41	0.22	0.56	0.38	0.08	0.17
20	13.7	10.7	0.99	3.26	1.37	1.63	0.77	0.84	1.37	1.60	0.89	1.95	2.31	0.82	2.14
30	14.9	12.7	1.13	3.53	1.62	1.94	0.94	1.02	1.86	2.16	1.17	2.38	3.00	1.34	2.74
40	14.7	13.0	1.12	3.42	1.65	1.97	0.96	1.04	2.05	2.36	1.25	2.46	3.18	1.63	2.88
50	14.1	12.8	1.08	3.23	1.61	1.91	0.95	1.02	2.10	2.40	1.27	2.42	3.18	1.76	2.86
60	13.4	12.3	1.02	3.03	1.55	1.83	0.92	0.98	2.09	2.38	1.25	2.34	3.11	1.78	2.78
70	12.7	11.8	0.97	2.84	1.49	1.74	0.88	0.94	2.05	2.32	1.21	2.25	3.02	1.74	2.69
80	12.0	11.3	0.92	2.67	1.42	1.65	0.84	0.90	2.00	2.26	1.18	2.16	2.91	1.68	2.59
90	11.5	10.8	0.87	2.51	1.36	1.57	0.81	0.86	1.94	2.19	1.14	2.07	2.80	1.61	2.48
100	10.9	10.4	0.83	2.37	1.30	1.50	0.78	0.83	1.88	2.12	1.10	1.99	2.70	1.53	2.39
200	7.42	7.24	0.56	1.54	0.91	1.02	0.55	0.58	1.40	1.56	0.80	1.39	1.94	0.99	1.69
300	5.69	5.62	0.43	1.15	0.70	0.78	0.42	0.45	1.12	1.24	0.63	1.08	1.52	0.72	1.32
400	4.65	4.62	0.35	0.93	0.58	0.6	0.35	0.37	0.94	1.03	0.52	0.89	1.26	0.57	1.09
500	3.96	3.95	0.30	0.78	0.49	0.54	0.30	0.32	0.81	0.89	0.45	0.76	1.08	0.48	0.93
600	3.46	3.46	0.26	0.67	0.43	0.48	0.26	0.28	0.71	0.78	0.40	0.66	0.95	0.41	0.82
700	3.08	3.09	0.23	0.60	0.38	0.42	0.23	0.25	0.64	0.70	0.35	0.59	0.85	0.36	0.73
800	2.78	2.79	0.21	0.53	0.35	0.38	0.21	0.22	0.58	0.64	0.32	0.53	0.77	0.32	0.66
900	2.53	2.55	0.19	0.48	0.32	0.35	0.19	0.21	0.54	0.59	0.29	0.49	0.71	0.29	0.61
1000	2.33	2.35	0.18	0.44	0.29	0.32	0.18	0.19	0.50	0.54	0.27	0.45	0.65	0.26	0.56
2000	1.34	1.36	0.10	0.25	0.17	0.18	0.10	0.11	0.29	0.32	0.16	0.26	0.38	0.14	0.32
3000	0.96	0.97	0.07	0.17	0.12	0.13	0.07	0.08	0.21	0.23	0.11	0.19	0.27	0.10	0.23
4000	0.75	0.77	0.06	0.14	0.09	0.10	0.06	0.06	0.17	0.18	0.09	0.15	0.22	0.08	0.18
5000	0.62	0.64	0.05	0.11	0.08	0.08	0.05	0.05	0.14	0.15	0.08	0.12	0.18	0.06	0.15

dipole-allowed transitions. The total GOSs for the excitations in the 9.93–12.17 eV range for H_2O and D_2O are consistent, as shown in Fig. 6(a). The experimental GOSs for corresponding bands are fitted with the Lassettre formula and the determined OOS data are compared with the photoabsorption measurements [11–14] in Table IV. The earliest absorption experiment reported in Ref. [11] includes the three highest bands and their data agree well with the present extrapolations. The latter measurement [12] reported more relevant OOSs and the data are consistent with the extrapolations except for the OOSs of bands VIII and XIII. The lower OOS data in Ref. [12] may be due to the second-order light as addressed by Lee and Suto [13]. The absorption experiments in Ref. [13] involved all the transition bands in this work and their data are generally in accord with the present extrapolations considering the respective error bars. The latest reported data in Ref. [14] are lower than the present extrapolations and previous absorption measurements, which might be attributed to some unknown systematic errors during their experiment [14].

As mentioned above, the experimental GOS profiles for the higher bands are characterized as typical dipole-allowed transitions which are applicable for the BE-scaling method. The integrated Born cross sections for electron impact excitations in these bands are scaled to an accurate level according to Eq. (6). The BE-scaled ICS data are listed in Table V and the total ICSs for the excitations in 9.93–12.17 eV for D_2O are compared with the data of H_2O in Fig. 6(b). In fact, electron impact excitation ICSs in a wide energy range are necessary input parameters for many applied sciences as the data for D_2O have not been available. The BE-scaling method can generate reliable ICS data for dipole-allowed excitations based on credible GOSs [25,26]. The BE-scaled ICSs reported in this work can supplement the molecular database with electron impact differential and integral cross sections for D_2O.

IV. CONCLUSION

In summary, generalized oscillator strengths for the $\tilde{A}\,^1B_1, \tilde{B}\,^1A_1, {}^1A_2 \leftarrow \tilde{X}\,^1A_1$ excitations and higher Rydberg transitions in 9.93–12.17 eV of heavy water were determined by fast electron scattering. The experimental measurements were performed by using an angle-resolved electron-energy-loss spectrometer with an incident electron energy of 1500 eV and an energy resolution of 80 meV. Crossed-beam-based relative flow technique facilitated the absolute normalization. The experimental GOSs for D_2O were generally consistent with the data of H_2O, while the appreciable discrepancy around the minimum for the $\tilde{A}\,^1B_1 \leftarrow \tilde{X}\,^1A_1$ transition remains unclear. Further theoretical investigations with nuclear effects are recommended to elucidate the issue. The comparisons with theoretical calculations under the FBA and SBA indicate that the contributions from higher-order Born terms become prominent for the experimental GOSs around the minima. Furthermore, the obtained OOSs by extrapolating the analytical fitted GOSs to $K^2 = 0$ provide an independent cross-check to previous photoabsorption and dipole (e, e) measurements. The BE-scaled ICSs for electron impact excitations were derived according to the analytical GOSs and the BE-scaling method. The relevant experimental data in this work can supplement the molecular database with accurate oscillator strengths and cross sections involving electron interactions with heavy water.

ACKNOWLEDGMENTS

This work was funded by the National Natural Science Foundation of China (Grants No. U1932207, No. 12104437, No. 12174259, and No. 11604003), the Natural Science Foundation of Anhui Province (Grant No. 2108085QA27), and Fundamental Research Funds for the Central Universities. W.-Q.X. also acknowledges support from the ShanghaiXFEL beamline project (SBP), the Shanghai Municipal Science and Technology Major Project (Grant No. 2017SHZDZX02), and the ShanghaiTech University High Performance Computing Public Service Platform.

---

[1] G. S. Timmins, Expert Opin. Ther. Pat. **24**, 1067 (2014).
[2] Z. Wang, B. S. Levison, J. E. Hazen, L. Donahue, X.-M. Li, and S. L. Hazen, Anal. Biochem. **455**, 35 (2014).
[3] H. Butner, S. Charnley, C. Ceccarelli, S. Rodgers, J. Pardo, B. Parise, J. Cernicharo, and G. Davis, Astrophys. J. **659**, L137 (2007).
[4] A. Yabushita, T. Hama, and M. Kawasaki, J. Photochem. Photobiol. C **16**, 46 (2013).
[5] B.-M. Cheng, E. P. Chew, C.-P. Liu, M. Bahou, Y.-P. Lee, Y. L. Yung, and M. Gerstell, Geophys. Res. Lett. **26**, 3657 (1999).
[6] M. Bahou, C.-Y. Chung, Y.-P. Lee, B.-M. Cheng, Y. L. Yung, and L. Lee, Astron. J. **559**, L179 (2001).
[7] J. Johns, Can. J. Phys. **41**, 209 (1963).
[8] S. Bell, J. Mol. Spectrosc. **16**, 205 (1965).
[9] H.-T. Wang, W. Felps, and S. McGlynn, J. Chem. Phys. **67**, 2614 (1977).
[10] E. Ishiguro, M. Sasanuma, H. Masuko, Y. Morioka, and M. Nakamura, J. Phys. B **11**, 993 (1978).
[11] D. Katayama, R. Huffman, and C. O'Bryan, J. Chem. Phys. **59**, 4309 (1973).
[12] P. Gürtler, V. Saile, and E.-E. Koch, Chem. Phys. Lett. **51**, 386 (1977).
[13] L. Lee and M. Suto, Chem. Phys. **110**, 161 (1986).
[14] J.-H. Fillion, J. Ruiz, X.-F. Yang, M. Castillejo, F. Rostas, and J.-L. Lemaire, J. Chem. Phys. **120**, 6531 (2004).
[15] B.-M. Cheng, C.-Y. Chung, M. Bahou, Y.-P. Lee, L. Lee, R. Van Harrevelt, and M. C. Van Hemert, J. Chem. Phys. **120**, 224 (2004).
[16] H. Bethe, Ann. Phys. (Leipzig) **397**, 325 (1930).
[17] E. N. Lassettre and A. Skerbele, J. Chem. Phys. **60**, 2464 (1974).
[18] N. Durante, U. Lamanna, G. Arrighini, and C. Guidotti, Theor. Chim. Acta **90**, 115 (1995).
[19] T. Giannerini, I. Borges, Jr., and E. Hollauer, J. Electron. Spectrosc. Relat. Phenom. **155**, 40 (2007).
[20] P. A. Thorn, M. J. Brunger, P. Teubner, N. Diakomichalis, T. Maddern, M. Bolorizadeh, W. Newell, H. Kato, M. Hoshino, H. Tanaka *et al.*, J. Chem. Phys. **126**, 064306 (2007).
[21] W.-Q. Xu, Z.-R. Ma, Y.-G. Peng, X.-J. Du, Y.-C. Xu, L.-H. Wang, B. Li, H.-R. Zhang, B.-Y. Zhang, J.-H. Zhu *et al.*, Phys. Rev. A **103**, 032808 (2021).
[22] W.-Q. Xu, Y.-G. Peng, J.-H. Zhu, X.-J. Du, Y.-C. Xu, L.-H. Wang, B. Li, H.-R. Zhang, B.-Y. Zhang, Z.-R. Ma, S.-X. Wang, Y. Wu, J.-G. Wang, and L.-F. Zhu, Phys. Rev. A **105**, 032801 (2022).
[23] E. N. Lassettre, J. Chem. Phys. **43**, 4479 (1965).
[24] L. Vriens, Phys. Rev. **160**, 100 (1967).
[25] H. Tanaka, M. J. Brunger, L. Campbell, H. Kato, M. Hoshino, and A. R. P. Rau, Rev. Mod. Phys. **88**, 025004 (2016).
[26] Y.-K. Kim, J. Chem. Phys. **126**, 064305 (2007).
[27] X.-J. Liu, L.-F. Zhu, X.-M. Jiang, Z.-S. Yuan, B. Cai, X.-J. Chen, and K.-Z. Xu, Rev. Sci. Instrum. **72**, 3357 (2001).
[28] Y.-W. Liu, L.-Q. Xu, D.-D. Ni, X. Xu, X.-C. Huang, and L.-F. Zhu, J. Geophys. Res.: Space Phys. **122**, 3459 (2017).
[29] J. Nickel, P. Zetner, G. Shen, and S. Trajmar, J. Phys. E **22**, 730 (1989).
[30] M. A. Khakoo and S. Trajmar, Phys. Rev. A **34**, 138 (1986).
[31] N. M. Cann and A. J. Thakkar, J. Electron. Spectrosc. Relat. Phenom. **123**, 143 (2002).
[32] X.-Y. Han and J.-M. Li, Phys. Rev. A **74**, 062711 (2006).
[33] B. P. Xie, L. F. Zhu, K. Yang, B. Zhou, N. Hiraoka, Y. Q. Cai, Y. Yao, C. Q. Wu, E. L. Wang, and D. L. Feng, Phys. Rev. A **82**, 032501 (2010).
[34] P. E. Grabowski and D. F. Chernoff, Phys. Rev. A **84**, 042505 (2011).
[35] M. Inokuti, Rev. Mod. Phys. **43**, 297 (1971).
[36] A. Rau and U. Fano, Phys. Rev. **162**, 68 (1967).
[37] W. P. Elderton, *Frequency Curves and Correlation* (Cambridge University Press, Cambridge, 2011).
[38] E. Malone, S. Petitto, and M. Langell, Solid State Commun. **130**, 571 (2004).
[39] G. Vankó and F. M. F. de Groot, Phys. Rev. B **75**, 177101 (2007).
[40] C. Schmidt, Geochim. Cosmochim. Acta **73**, 425 (2009).
[41] H.-C. Tian, L.-Q. Xu, and L.-F. Zhu, Chin. Phys. B **27**, 043101 (2018).
[42] L.-F. Zhu, H.-C. Tian, Y.-W. Liu, X. Kang, and G.-X. Liu, Chin. Phys. B **24**, 043101 (2015).
[43] R. P. McEachran, M. Vos, and L.-F. Zhu, Phys. Rev. A **87**, 052703 (2013).
[44] N. Watanabe and M. Takahashi, J. Phys. B **53**, 075202 (2020).
[45] S.-X. Wang, X.-J. Du, Q. Sun, Y.-W. Liu, D.-G. Qi, and L.-F. Zhu, J. Quant. Spectrosc. Radiat. Transfer **277**, 107988 (2022).
[46] N. Watanabe and M. Takahashi, J. Phys. B **55**, 015201 (2022).
[47] C.-Y. Chung, E. P. Chew, B.-M. Cheng, M. Bahou, and Y.-P. Lee, Nucl. Instrum. Methods Phys. Res. Sect. A **467–468**, 1572 (2001).
[48] W. Chan, G. Cooper, and C. Brion, Chem. Phys. **178**, 387 (1993).
[49] K. Yoshino, J. Esmond, W. Parkinson, K. Ito, and T. Matsui, Chem. Phys. **211**, 387 (1996).
[50] M.-Y. Song, H. Cho, G. P. Karwasz, V. Kokoouline, Y. Nakamura, J. Tennyson, A. Faure, N. J. Mason, and Y. Itikawa, J. Phys. Chem. Ref. Data **50**, 023103 (2021).
[51] L. Hargreaves, K. Ralphs, G. Serna, M. Khakoo, C. Winstead, and V. McKoy, J. Phys. B **45**, 201001 (2012).